


**Higher-order topological corner and bond-localized modes in magnonic insulators**Sayak Bhowmik,<sup>1,2,\*</sup> Saikat Banerjee<sup>3,4,†</sup> and Arijit Saha<sup>1,2,‡</sup><sup>1</sup>*Institute of Physics, Sachivalaya Marg, Bhubaneswar, Orissa 751005, India*<sup>2</sup>*Homi Bhabha National Institute, Training School Complex, Anushakti Nagar, Mumbai 400094, India*<sup>3</sup>*Theoretical Division, T-4, Los Alamos National Laboratory, Los Alamos, New Mexico 87545, USA*<sup>4</sup>*Center for Materials Theory, Rutgers University, Piscataway, New Jersey 08854, USA* (Received 28 October 2023; revised 11 February 2024; accepted 4 March 2024; published 18 March 2024)

We theoretically investigate a two-dimensional decorated honeycomb lattice framework to realize a second-order topological magnon insulator (SOTMI) phase featuring distinct corner-localized modes. Our study emphasizes the pivotal role of spin-magnon mapping in characterizing bosonic topological properties, which exhibit differences from their fermionic counterparts. We employ a symmetry indicator topological invariant to identify and characterize this SOTMI phase, particularly for systems respecting time-reversal and  $C_6$  rotational symmetry. Using a spin model defined on a honeycomb lattice geometry, we demonstrate that introducing “*kekulé*” type distortions yields a topological phase. In contrast, “*antikekulé*” distortions result in a nontopological magnonic phase. The presence of *kekulé* distortions manifests in two distinct topologically protected bosonic corner modes—an *intrinsic* and a *pseudo*, based on the specific edge terminations. On the other hand, *antikekulé* distortions give rise to Tamm/Shockley type bond-localized boundary modes, which are nontopological and reliant on particular edge termination. We further investigate the effects of random out-of-plane exchange anisotropy disorder on the robustness of these bosonic corner modes. The distinction between SOTMIs and their fermionic counterparts arises due to the system-specific magnonic onsite energies, a crucial feature often overlooked in prior literature. Our study unveils exciting prospects for engineering higher-order topological phases in magnon systems and enhances our understanding of their unique behavior within decorated honeycomb lattices.

DOI: [10.1103/PhysRevB.109.104417](https://doi.org/10.1103/PhysRevB.109.104417)

**Introduction.** Since the discovery of graphene [1,2] and the advent of topological insulators [3], non-Bravais lattices have become a central platform for exploring exotic quantum phenomena in contemporary condensed matter physics. On one front, extensive research has been dedicated to the topological classification of noninteracting systems, encompassing both symmorphic [4,5] and nonsymmorphic crystalline structures [6–8], over the past decade. On the other hand, the focus has shifted towards extending these concepts into the realm of correlated electron systems, notably in topological Mott [9–11] and Kondo insulators [12,13].

Among the various non-Bravais lattices, honeycomb lattice is one of the simplest examples because of its abundance in various quantum materials, that accomodates intricate multiband physics without strong interactions. While it is renowned for its fermionic Dirac excitations and topological quasiparticles, recent research has extended its significance to encompass bosonic systems featuring novel topological band structures. These advances have spurred the exploration of diverse bosonic topological materials, spanning photonic crystals [14,15], plasmonic systems [16,17], arrays of superconducting grains [18], and magnetic structures [19–21],

etc. and opened up a new and compelling avenue for scientific inquiry. Recently, higher-order topological insulators (HOTI) have gained significant attention as a novel and intriguing class of systems—extended for both fermionic [22–36] and bosonic platform [37–42]. In a  $d$ -dimensional space, an  $n$ th-order HOTI is characterized by the presence of  $(d - n)$  dimensional boundary modes. More specifically, two-dimensional (2D) second-order topological magnon insulators (SOTMI) exhibit a distinct presence of a finite number of corner modes. Previous theoretical investigations into various systems ranging from the breathing kagome and square lattices [43,44] to skyrmion crystals [37], and twisted bilayer honeycomb networks [45] have demonstrated the existence of such topologically protected magnonic corner modes. An important ingredient in most of these previous magnonic works is the presence of Dzyaloshinskii-Moriya interaction [46]. However, the latter is only present in noncentrosymmetric systems and is related to the underlying spin-orbit coupling [47]—which can be substantially small in real materials. Furthermore, specific details of the *spin-magnon* mapping play an important role in finite-size bosonic systems, which is typically absent in the fermionic counterparts. Bosonic excitations carry a distinct feature—they must be positive definite. This unique characteristic results in specific onsite terms in the spin-magnon mapping. To the best of our knowledge, this fact has not been effectively considered in the previous studies [20] as far as higher-order topology is concerned.

\*sayak.bhowmik@iopb.res.in

†saikat.banerjee@rutgers.edu

‡arijit@iopb.res.in

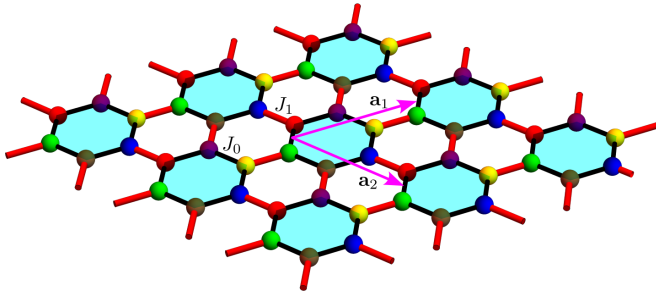


FIG. 1. Schematic representation of a 2D honeycomb-lattice model with a six-site unit cell (depicted by colored hexagons). The black bonds represent ferromagnetic coupling with strength  $J_0$ , while the red bonds indicate coupling with strength  $J_1$ . The lattice vectors  $\mathbf{a}_1$  and  $\mathbf{a}_2$  are shown, along with the sublattice sites (distinguished by six different colors) as labeled in the figure.

Due to the reasons outlined above, here, we focus on a centrosymmetric ferromagnetic (FM) system within a decorated 2D honeycomb lattice configuration, as shown in Fig. 1. This setup can be envisioned as an extension of the one-dimensional Su-Schrieffer-Heeger model. Within this context, two distinct distortion scenarios naturally emerge—one where the inter-unit cell coupling surpasses the coupling within a unit cell ( $J_0 < J_1$ ), resulting in a kekulé structure; the alternate scenario entails an antikekulé distortion, arising when the opposite limit is considered [48]. In our study of the kekulé structure, we identify two distinct SOTMI phases. The first is a *intrinsic* SOTMI phase, which features conventional protected corner modes. The second is a *pseudo*-SOTMI phase that emerges when the system is truncated differently. Surprisingly, we also discover bond-localized magnon modes in the antikekulé structure. We analyze the effects of disorder to assess the robustness of these characteristic boundary states. Our findings indicate that the boundary modes in the kekulé configuration are resilient, while the bond-localized modes are not.

*Model and method.* The system of our interest involves nearest neighbor Heisenberg spin exchange interactions on a decorated honeycomb lattice comprising of six sublattices with intracell (intercell) exchange couplings denoted by  $J_0$  ( $J_1$ ) (see Fig. 1). The corresponding Hamiltonian is given by

$$\mathcal{H} = - \sum_{\langle ij \rangle} J_{ij} \mathbf{S}_i \cdot \mathbf{S}_j - \beta \sum_i (S_i^z)^2, \quad (1)$$

where,  $J_{ij}$ 's are equal to  $J_0$  or  $J_1$  depending on the bond types, and  $\beta > 0$  signifies the strength of the onsite single-ion anisotropy. Note that, we account for the onsite anisotropy term as the Mermin-Wagner theorem prohibits long-range magnetic ordering in two dimensions. To obtain the magnon picture in the linear spin-wave regime, we carry out the spin-magnon mapping by performing Holstein-Primakoff transformation on the FM ground state, given by

$$S_i^+ \approx \sqrt{2S} \eta_{i\alpha}, \quad S_i^- \approx \sqrt{2S} \eta_{i\alpha}^\dagger, \quad S_i^z = (S - \eta_{i\alpha}^\dagger \eta_{i\alpha}). \quad (2)$$

Here,  $S_i^\pm = S_i^x \pm iS_i^y$ , are the raising and lowering operators, and  $\eta_{i\alpha}^\dagger$  creates a magnon excitation at site  $i$ . Since we have six sublattice sites, there are six flavors ( $\alpha = 1, \dots, 6$ ) of magnon

operators. The corresponding bosonic Hamiltonian reads as  $\mathcal{H} = \mathcal{H}_0 + \mathcal{H}_1$ , where

$$\mathcal{H}_0 = S \sum_{\langle ij \rangle} J_{ij} (\eta_i^\dagger \eta_i + \eta_j^\dagger \eta_j) + 2\beta S \sum_i \eta_i^\dagger \eta_i, \quad (3a)$$

$$\mathcal{H}_1 = -S \sum_{\langle ij \rangle} J_{ij} (\eta_i^\dagger \eta_j + \text{H.c.}). \quad (3b)$$

Here,  $\mathcal{H}_0$  corresponds to the onsite part, and  $\mathcal{H}_1$  denotes the magnon hopping contribution to the total Hamiltonian. The dependence on the sublattice degrees of freedom is implicitly assumed. Furthermore,  $J_{ij} > 0$  is a necessary constraint needed to ensure FM order. The first term of the Hamiltonian in Eq. (3a) indicates bond-dependent onsite energy highlighting an intrinsic property of *magnonic* Hamiltonians in contrast to the usual *fermionic* tight-binding Hamiltonians. The onsite energy depends on the number of neighboring bonds, and hence is different for the bulk and the boundary sites. This plays a crucial role in determining the nature of the boundary modes for finite systems, as we explain in more detail in the following text.

*Realization of SOTMI phase and its topological characterization.* Assuming translational invariance, the Hamiltonian in Eqs. (3a) and (3b) can be written in momentum space as  $\mathcal{H} = \sum_{\mathbf{k}} \psi_{\mathbf{k}}^\dagger \mathcal{H}_{\mathbf{k}} \psi_{\mathbf{k}}$ , where  $\mathcal{H}_{\mathbf{k}}$  is a  $6 \times 6$  matrix having basis  $\psi_{\mathbf{k}} = (\eta_{\mathbf{k},1}, \eta_{\mathbf{k},2}, \eta_{\mathbf{k},3}, \eta_{\mathbf{k},4}, \eta_{\mathbf{k},5}, \eta_{\mathbf{k},6})^\top$  (see Ref. [49] for details). It is easy to check that  $\mathcal{H}_{\mathbf{k}}$  respects time-reversal symmetry:  $\mathcal{H}_{\mathbf{k}}^* = \mathcal{H}_{-\mathbf{k}}$ , inversion symmetry  $\mathcal{P} = \sigma_x \otimes \mathcal{I}_3$ :  $\mathcal{P}^{-1} \mathcal{H}_{\mathbf{k}} \mathcal{P} = \mathcal{H}_{-\mathbf{k}}$  along with a sixfold rotational ( $\mathbf{C}_6$ ) symmetry:  $U_{\mathbf{C}_6}^\dagger \mathcal{H}_{\mathbf{k}} U_{\mathbf{C}_6} = \mathcal{H}_{\mathbf{C}_6 \mathbf{k}}$ . Here,  $U_{\mathbf{C}_6}$  corresponds to the unitary operator representation for  $\mathbf{C}_6$  rotation and  $\sigma_x, \mathcal{I}_3$  denote Pauli matrix and Identity matrix, respectively [49]. Under these symmetry considerations, we adopt the well-developed mathematical framework of symmetry indicator topological invariant [22,24,50,51] to characterize of higher-order topology of the magnonic system. Considering the  $\mathbf{C}_6$  symmetry we label this invariant as  $\chi^{(6)}$  (see the details in Ref. [49]).

The magnon band structure is obtained by diagonalizing  $\mathcal{H}_{\mathbf{k}}$ . We notice that for  $J_0 \neq J_1$ , the bulk spectrum is gapped at finite energy in the mid-band region (between the third and the fourth band) [49]. Note that the gap opens at  $\Gamma$  point in contrast to the conventional Dirac point for graphene. In this case, we obtain an analytical expression for the associated bulk gap as  $\Delta = 2S|J_0 - J_1|$ . Consequently,  $\mathcal{H}_{\mathbf{k}}$  goes through a gap-closing transition at  $\mathbf{k} = \Gamma$  for  $J_0 = J_1$  [49], which is at the middle of the magnon bandwidth. Furthermore, when  $J_0 > 1.32J_1$ , a secondary trivial bulk gap appears away from the mid band region both at low energy (between the first and the second band) and high energy (between the fifth and the sixth band).

To appropriately distinguish the SOTMI phase from the trivial gapped phase, we employ the symmetry indicator integer topological invariant  $\chi^{(6)}$  for proper characterization of the magnon Bloch bands [50]. Here,  $\chi^{(6)}$  is constructed by utilizing the previously mentioned symmetries of  $\mathcal{H}_{\mathbf{k}}$  as well as the symmetries of the high-symmetry points in the Brillouin zone (see Ref. [49] for details).  $\chi^{(6)} \neq 0$  identifies the SOTMI phase that ensures the presence of topologically protected magnon corner modes (MCMs), while the trivial phase is marked by  $\chi^{(6)} = 0$ . Our system displays the SOTMI phase

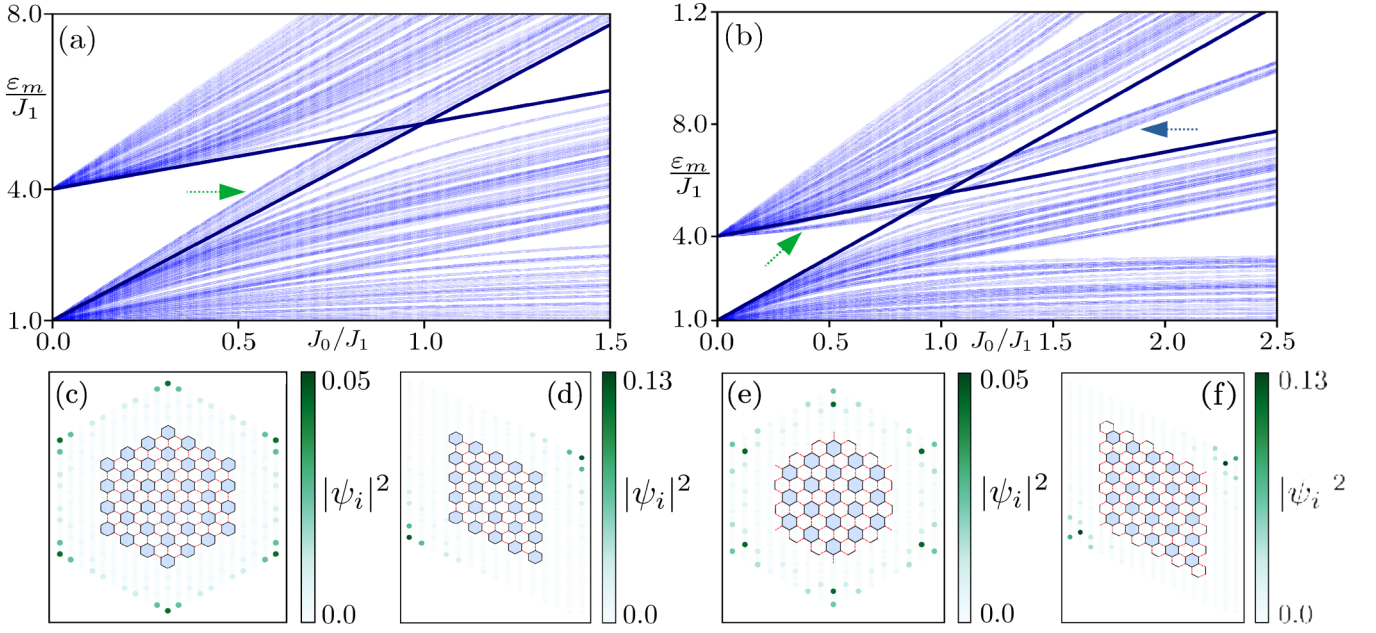


FIG. 2. Numerical results for a finite-size system are illustrated employing open boundary conditions (OBC). (a) and (b) depict the magnon eigenvalue spectra as a function of  $J_0/J_1$  for hexagonal geometries corresponding to the lattice structures depicted in the insets of (c) and (e), respectively. The dark blue lines in the spectra represent the two energy eigenvalues of  $\mathcal{H}_{\mathbf{k}}$  at  $\mathbf{k} = \Gamma$ , identifying the magnon bulk gap  $\Delta$ . (c) and (d) illustrate site-resolved normalized probabilities ( $|\psi_i|^2$ ) of in-gap states contributing to MCMs for  $J_0 = 0.7$ , with the respective lattice geometries shown in the insets.  $|\psi_i|^2$  is averaged over six (two) states contributing to MCMs for hexagonal (rhombus) geometry. (e) and (f) depict the averaged site-resolved normalized probabilities of in-gap states representing the pseudo corner modes for  $J_0 = 0.7$ , with the corresponding lattice geometries displayed in the insets. The finite-size lattice geometries in (c) and (d) consist of 222 sites (37 unit cells) and 150 sites (25 unit cells), respectively, representing the intrinsic SOTMI phase. The lattice geometries in (e) and (f) consist of 144 sites (12 outer-edge bonds) and 192 sites (20 outer-edge bonds), respectively, demonstrating the pseudo SOTMI phase. Other model parameters are chosen as  $(J_1, \beta, S) = (1, \frac{1}{3}, \frac{3}{2})$ .

hosting topologically protected MCMs in the regime  $J_0 < J_1$  (kekulé structure) with  $\chi^{(6)} = 2$ . In addition, we rule out the signatures of any first-order topological phase by computing the appropriate topological invariant [22,24,52] (see Ref. [49] for the details).

*Emergence of topologically protected MCMs in finite-size systems.* We capture the topological characteristics of the SOTMI phase hosting the MCMs by applying open boundary conditions (OBCs) and performing numerical calculations based on the finite-size 2D lattice geometry. In this context, two distinct lattice geometries are considered: *hexagonal*, and *rhombus* having six and two corners, respectively (see the insets in Fig. 2). A few remarks are necessary at this stage. (i) As a result of bond-dependent onsite energy, the first term in Eq. (3a) readily generates an onsite energy difference (OED) between the bulk and the boundary by an amount  $SJ_1$ , and (ii) the OED reflects how the edges are terminated in different geometries. Such a feature is generally absent in a similar fermionic system.

The energy eigenvalue spectrum as a function of  $J_0/J_1$  is obtained by diagonalizing the Hamiltonian in Eqs. (3a) and (3b) with OBC [see Fig. 2(a)]. Note that the spectrum originates from the finite value because of a finite onsite anisotropy term with finite  $\beta$ . In the region  $J_0 < J_1$  (kekulé structure), there exists identifiable in-gap states demonstrating topologically protected MCMs, whereas there exists no in-gap states when  $J_0 > J_1$  (antikekulé structure). This reflects

consistency with the obtained value of  $\chi^{(6)}$ . Additionally, the in-gap states are closer to the lower bulk states for  $J_0 \ll J_1$  while they are closer to both the upper and lower bulk states when  $J_0 \lesssim J_1$ . The states immediately below the upper bulk states [indicated by the arrow in Fig. 2(a)] contribute to the MCMs. This reflects the consequence of OED and reveals a true *magnonic* signature distinguishing it from the regular *fermionic* systems, where one would readily expect the topologically protected in-gap states to appear precisely in the middle of the bulk gap. Specifically, we obtain six (two) states that exhibit MCM signatures while considering hexagonal (rhombus) lattice geometry. We depict the localized MCMs by the normalized site-resolved probability  $|\psi_i|^2$  of the particular in-gap states in Figs. 2(c) and 2(d), with respective lattice geometry illustrated in the inset. The other in-gap states do not contribute to the MCMs and are not zero-dimensional. A few of them are shown in Ref. [49], and resembles fractal like structures. However, we skip the discussion on these states as it is beyond the scope of the present paper.

Thus far, our finite-size analysis has followed a specific termination scheme, ensuring that individual unit cells remain intact (type I), as demonstrated in the insets of Figs. 2(c) and 2(d). This arrangement leads to what we call the *intrinsic* SOTMI phase, for which the results of our numerical analysis have been displayed in Figs. 2(a), 2(c) and 2(d). However, another scenario, type II, naturally emerges when the

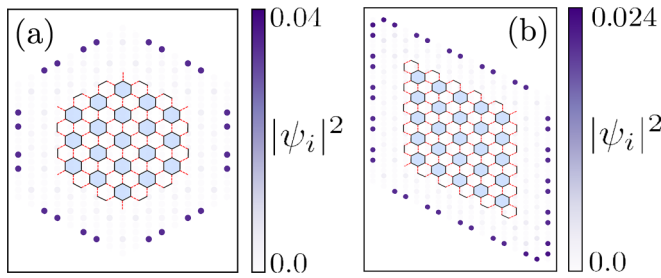


FIG. 3. Site-resolved normalized probability distributions of in-gap states illustrating *Tamm/Shockley* type BLMMs for  $J_0 = 2.0$ , shown in (a) and (b) for hexagonal and rhombus geometries, respectively. The lattice geometries in (a) and (b) consist of 144 sites (12 outer-edge bonds) and 192 sites (20 outer-edge bonds), respectively. Other model parameters are chosen as  $(J_1, \beta, S) = (1, \frac{1}{3}, \frac{3}{2})$ .

sample edges are terminated differently, resulting in incomplete unit cells. In this configuration, there are six (two) sites at the corners with single bonds for the hexagonal (rhombus) geometry, as depicted in the insets of Figs. 2(e) and 2(f). This arrangement gives rise to a *pseudo*-SOTMI phase, originating from the in-gap states present in the topological region ( $J_0 < J_1$ ), as indicated by the green arrow in Fig. 2(b). Analyzing the site-resolved normalized probability of these states for both geometries, it becomes clear that these states do not exhibit robust localization exclusively at the corners [see Figs. 2(e) and 2(f)]. Instead, they display partial localization, with the highest probability contribution occurring at the sites coupled to the corners. This observation justifies the term *pseudo* SOTMI phase. As explained earlier, this analysis differs significantly from previously reported theoretical work on an analogous fermionic system [48]. Further analyzing the magnon spectrum in the type II scenario and as a function of  $J_0/J_1$  in the nontopological regime ( $J_0 > J_1$ ) [see Fig. 2(b)], we note that there also exist in-gap states. The number of these in-gap states depends on the system size and geometry, precisely matching the number of bonds constituting the outer edge of the finite system. They lead to interesting geometric *Tamm/Shockley* type bond-localized magnon modes (BLMMs). These BLMMs can be visualized through the  $|\psi_i|^2$  of the in-gap states depicted in Figs. 3(a) and 3(b), corresponding to the respective lattice geometry shown in the inset. However, they lack any topological protection as  $\chi^{(6)} = 0$  in this case.

Note that the apparent asymmetry of the in-gap states in Figs. 2(a) and 2(b) is a direct consequence of the OED as mentioned earlier. This is in stark contrast to its fermionic analogs where typically the in-gap states are positioned at the middle of bulk gaps for particle-hole symmetric systems.

*Effect of disorder and stability analysis for MCMs.* Up to this point, we discuss both the topological and nontopological characteristics of the honeycomb network by considering clean (disorder-free) limits. However, real materials are prone to impurities and disorder. Consequently, without aiming for a specific material realization, we focus on a generic disorder by considering a random out-of-plane exchange anisotropy. The Hamiltonian in Eq. (1) is therefore modified as

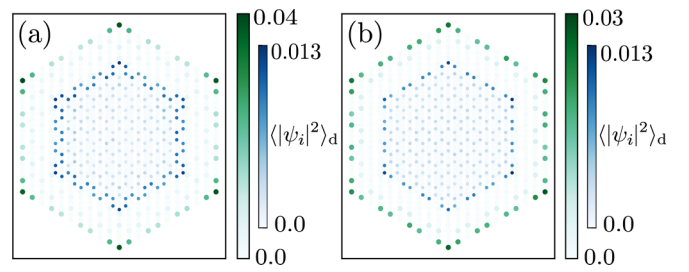


FIG. 4. Disorder-averaged site-resolved probability distribution  $\langle |\psi_i|^2 \rangle_d$  of states leading to MCMs is depicted in the intrinsic SOTMI phase. (a) Depicts case I for  $\zeta = 0.8$  and  $J_0 = 0.7$ , with the inset corresponding to  $\zeta = 0.8$  and  $J_0 = 0.4$ . (b) Illustrates case II for  $\zeta = 0.3$  and  $J_0 = 0.3$ , with the inset displaying for  $\zeta = 0.7$  and  $J_0 = 0.7$ . We choose the other model parameter values as  $(J_1, \beta, S) = (1, \frac{1}{3}, \frac{3}{2})$ .

$\mathcal{H} \Rightarrow \mathcal{H} + \mathcal{H}_{\text{dis}}$ , where

$$\mathcal{H}_{\text{dis}} = - \sum_{\langle ij \rangle} J_{ij}^d S_i^z S_j^z. \quad (4)$$

Here,  $J_{ij}^d$  is a random coupling parameter uniformly distributed in the range  $[-\zeta, \zeta]$  with  $\zeta$  being the disorder strength. Ensuring FM order in the presence of disorder readily imposes the following constraint:  $\zeta_{\text{max}} = J_0(J_1)$  for intra (inter) cell exchange coupling. Remarkably, the out-of-plane exchange disorder mentioned in Eq. (4) leads to an effective bond-dependent on-site disorder for the bosonic case. This translates into a disordered magnon Hamiltonian where we substitute  $J_{ij}$  by  $J_{ij} + J_{ij}^d$  in Eq. (3a).

In the subsequent discussions, we focus primarily on the *intrinsic* SOTMI phase by investigating the stability of the MCMs (magnon corner modes) in the presence of such a disorder, as mentioned earlier. The qualitative features of the *pseudo* SOTMI phase remain identical to the previous case. We analyze the disorder-averaged site-resolved probability  $\langle |\psi_i|^2 \rangle_d$  for specific states while varying the disorder strength  $\zeta$ . We investigate two cases with distinct characteristics:

Case I. Disorder in the intercell coupling  $J_1$ . In this scenario, the system continues to exhibit MCM signatures for higher values of  $J_0$  even for higher disorder strength  $\zeta$  [see Fig. 4(a)].

Case II. Disorder in the intracell coupling  $J_0$ . Here, the system tends to exhibit outer-edge bond localization when the disorder is introduced [see Fig. 4(b)].

For both cases, the MCMs are more susceptible to the disorder effects for smaller  $J_0$  than a larger value with the same disorder strength. This observation arises from the fact that the in-gap states, responsible for the emergence of MCMs, at lower  $J_0$  values are closer to the bulk states [see Fig. 2(a)]. Consequently, these MCMs tend to hybridize with the bulk states even in the presence of relatively mild disorder and is eventually destroyed. We refer the readers to Ref. [49] for the discussion of stability analysis of MCMs in the case of rhombus geometry.

*Summary and discussion.* To summarize, in this paper, we introduce a FM honeycomb lattice network that enables the realization of a higher-order bosonic topological system. Our findings are particularly relevant to centrosymmetric systems

and underscore the crucial role of spin-magnon mapping in generating both an intrinsic and a pseudo SOTMI phase, each characterized by appropriate topological invariant and unique boundary modes. In this context, our work stands in stark contrast to a previous theoretical study [53], which explores a similar system under noncentrosymmetric conditions. While intrinsic SOTMI phases have been previously discussed in magnonic systems (square lattice) in the presence of anti-skyrmions [37,38], our study exhibiting the emergence of both intrinsic and pseudo SOTMI phase in a simple magnonic model system carries significant contribution, to the best of our knowledge.

Moreover, we have explored the robustness of the boundary modes within the topological phase under the influence of random disorder. Specifically, we model the disorder arising from out-of-plane exchange anisotropy and provide qualitative estimates of the topological robustness of MCMs across varying disorder strengths. It is worth noting that during the preparation of this manuscript, we became aware of a recent theoretical work [47], where the authors investigated a differ-

ent disorder realization involving onsite magnetic fields. Our work complements this research by offering insights into a more realistic scenario through an exchange anisotropy disorder. From a practical point of view, the spatial distribution of the localized MCMs can possibly be measured by nitrogen-vacancy center magnetometry [54] or near-field Brillouin light scattering [55]. Overall, our findings hold promise for advancing robust future magnonic devices.

*Acknowledgments.* We thank Jason T. Haraldsen and Ying Su for providing important feedback while preparing the manuscript. Sayak Bhowmik (S.B.) and A.S. acknowledge the SAMKHYA: HPC Facility provided at IOP, Bhubaneswar, for numerical computations. Saikat Banerjee (S.B.) acknowledges support from the U.S. Department of Energy (DOE), Office of Science, and Office of Advanced Scientific Computing Research through the Quantum Internet to Accelerate Scientific Discovery Program, and partial support from the Office of Basic Energy Sciences, Material Sciences and Engineering Division, U.S. DOE under Contract No. DE-FG02-99ER45790.

- 
- [1] A. H. Castro Neto, F. Guinea, N. M. R. Peres, K. S. Novoselov, and A. K. Geim, The electronic properties of graphene, *Rev. Mod. Phys.* **81**, 109 (2009).
- [2] V. N. Kotov, B. Uchoa, V. M. Pereira, F. Guinea, and A. H. Castro Neto, Electron-electron interactions in graphene: Current status and perspectives, *Rev. Mod. Phys.* **84**, 1067 (2012).
- [3] M. Z. Hasan and C. L. Kane, Colloquium: Topological insulators, *Rev. Mod. Phys.* **82**, 3045 (2010).
- [4] S. A. Parameswaran, A. M. Turner, D. P. Arovas, and A. Vishwanath, Topological order and absence of band insulators at integer filling in non-symmorphic crystals, *Nat. Phys.* **9**, 299 (2013).
- [5] Z. Zhu, G. W. Winkler, Q. Wu, J. Li, and A. A. Soluyanov, Triple point topological metals, *Phys. Rev. X* **6**, 031003 (2016).
- [6] C.-X. Liu, R.-X. Zhang, and B. K. VanLeeuwen, Topological nonsymmorphic crystalline insulators, *Phys. Rev. B* **90**, 085304 (2014).
- [7] C. Fang and L. Fu, New classes of three-dimensional topological crystalline insulators: Nonsymmorphic and magnetic, *Phys. Rev. B* **91**, 161105(R) (2015).
- [8] S. Banerjee and A. Saxena, Higher chern numbers in multilayer lieb lattices ( $n \geq 2$ ): Topological transitions and quadratic band crossing lines, *Phys. Rev. B* **103**, 235125 (2021).
- [9] J. Maciejko and G. A. Fiete, Fractionalized topological insulators, *Nat. Phys.* **11**, 385 (2015).
- [10] M. Z. Hasan and J. E. Moore, Three-dimensional topological insulators, *Annu. Rev. Condens. Matter Phys.* **2**, 55 (2011).
- [11] S. Rachel, Interacting topological insulators: A review, *Rep. Prog. Phys.* **81**, 116501 (2018).
- [12] M. Dzero, K. Sun, V. Galitski, and P. Coleman, Topological kondo insulators, *Phys. Rev. Lett.* **104**, 106408 (2010).
- [13] M. Dzero, J. Xia, V. Galitski, and P. Coleman, Topological kondo insulators, *Annu. Rev. Condens. Matter Phys.* **7**, 249 (2016).
- [14] F. D. M. Haldane and S. Raghu, Possible realization of directional optical waveguides in photonic crystals with broken time-reversal symmetry, *Phys. Rev. Lett.* **100**, 013904 (2008).
- [15] F. Liu, H.-Y. Deng, and K. Wakabayashi, Topological photonic crystals with zero berry curvature, *Phys. Rev. B* **97**, 035442 (2018).
- [16] G. Weick, C. Woollacott, W. L. Barnes, O. Hess, and E. Mariani, Dirac-like plasmons in honeycomb lattices of metallic nanoparticles, *Phys. Rev. Lett.* **110**, 106801 (2013).
- [17] X. Wu, Y. Meng, J. Tian, Y. Huang, H. Xiang, D. Han, and W. Wen, Direct observation of valley-polarized topological edge states in designer surface plasmon crystals, *Nat. Commun.* **8**, 1304 (2017).
- [18] S. Banerjee, J. Fransson, A. M. Black-Schaffer, H. Ågren, and A. V. Balatsky, Granular superconductor in a honeycomb lattice as a realization of bosonic dirac material, *Phys. Rev. B* **93**, 134502 (2016).
- [19] J. Fransson, A. M. Black-Schaffer, and A. V. Balatsky, Magnon dirac materials, *Phys. Rev. B* **94**, 075401 (2016).
- [20] S. S. Pershoguba, S. Banerjee, J. C. Lashley, J. Park, H. Ågren, G. Aepli, and A. V. Balatsky, Dirac magnons in honeycomb ferromagnets, *Phys. Rev. X* **8**, 011010 (2018).
- [21] P. A. McClarty, Topological magnons: A review, *Annu. Rev. Condens. Matter Phys.* **13**, 171 (2022).
- [22] W. A. Benalcazar, B. A. Bernevig, and T. L. Hughes, Quantized electric multipole insulators, *Science* **357**, 61 (2017).
- [23] F. Schindler, A. M. Cook, M. G. Vergniory, Z. Wang, S. S. P. Parkin, B. A. Bernevig, and T. Neupert, Higher-order topological insulators, *Sci. Adv.* **4**, eaat0346 (2018).
- [24] W. A. Benalcazar, B. A. Bernevig, and T. L. Hughes, Electric multipole moments, topological multipole moment pumping, and chiral hinge states in crystalline insulators, *Phys. Rev. B* **96**, 245115 (2017).
- [25] J. Langbehn, Y. Peng, L. Trifunovic, F. von Oppen, and P. W. Brouwer, Reflection-symmetric second-order topological insulators and superconductors, *Phys. Rev. Lett.* **119**, 246401 (2017).
- [26] S. Franca, J. van den Brink, and I. C. Fulga, An anomalous higher-order topological insulator, *Phys. Rev. B* **98**, 201114(R) (2018).

- [27] Z. Wang, B. J. Wieder, J. Li, B. Yan, and B. A. Bernevig, Higher-order topology, monopole nodal lines, and the origin of large fermi arcs in transition metal dichalcogenides  $XTe_2$  ( $X = Mo, W$ ), *Phys. Rev. Lett.* **123**, 186401 (2019).
- [28] M. Geier, L. Trifunovic, M. Hoskam, and P. W. Brouwer, Second-order topological insulators and superconductors with an order-two crystalline symmetry, *Phys. Rev. B* **97**, 205135 (2018).
- [29] D. Călugăru, V. Juričić, and B. Roy, Higher-order topological phases: A general principle of construction, *Phys. Rev. B* **99**, 041301(R) (2019).
- [30] M. Ezawa, Higher-order topological insulators and semimetals on the breathing kagome and pyrochlore lattices, *Phys. Rev. Lett.* **120**, 026801 (2018).
- [31] B. Roy, Antiunitary symmetry protected higher-order topological phases, *Phys. Rev. Res.* **1**, 032048(R) (2019).
- [32] L. Trifunovic and P. W. Brouwer, Higher-order bulk-boundary correspondence for topological crystalline phases, *Phys. Rev. X* **9**, 011012 (2019).
- [33] E. Khalaf, Higher-order topological insulators and superconductors protected by inversion symmetry, *Phys. Rev. B* **97**, 205136 (2018).
- [34] B. Xie, H. X. Wang, X. Zhang, P. Zhan, J. H. Jiang, M. Lu, and Y. Chen, Higher-order band topology, *Nat. Rev. Phys.* **3**, 520 (2021).
- [35] L. Trifunovic and P. W. Brouwer, Higher-order topological band structures, *Phys. Status Solidi B* **258**, 2000090 (2021).
- [36] F. Schindler, Dirac equation perspective on higher-order topological insulators, *J. Appl. Phys.* **128**, 221102 (2020).
- [37] T. Hirofusa, S. A. Díaz, J. Klinovaja, and D. Loss, Magnonic quadrupole topological insulator in antiskyrmion crystals, *Phys. Rev. Lett.* **125**, 207204 (2020).
- [38] A. Mook, S. A. Díaz, J. Klinovaja, and D. Loss, Chiral hinge magnons in second-order topological magnon insulators, *Phys. Rev. B* **104**, 024406 (2021).
- [39] Z. Li, Y. Cao, P. Yan, and X. Wang, Higher-order topological solitonic insulators, *npj Comput. Mater.* **5**, 107 (2019).
- [40] Y. You, T. Devakul, F. J. Burnell, and T. Neupert, Higher-order symmetry-protected topological states for interacting bosons and fermions, *Phys. Rev. B* **98**, 235102 (2018).
- [41] O. Dubinkin and T. L. Hughes, Higher-order bosonic topological phases in spin models, *Phys. Rev. B* **99**, 235132 (2019).
- [42] J. Bibo, I. Lovas, Y. You, F. Grusdt, and F. Pollmann, Fractional corner charges in a two-dimensional superlattice bose-hubbard model, *Phys. Rev. B* **102**, 041126(R) (2020).
- [43] A. Sil and A. K. Ghosh, First and second order topological phases on ferromagnetic breathing kagome lattice, *J. Phys.: Condens. Matter* **32**, 205601 (2020).
- [44] Z.-X. Li, Y. Cao, X. R. Wang, and P. Yan, Second-order topological solitonic insulator in a breathing square lattice of magnetic vortices, *Phys. Rev. B* **101**, 184404 (2020).
- [45] C.-B. Hua, F. Xiao, Z.-R. Liu, J.-H. Sun, J.-H. Gao, C.-Z. Chen, Q. Tong, B. Zhou, and D.-H. Xu, Magnon corner states in twisted bilayer honeycomb magnets, *Phys. Rev. B* **107**, L020404 (2023).
- [46] I. Dzyaloshinsky, A thermodynamic theory of “weak” ferromagnetism of antiferromagnetics, *J. Phys. Chem. Solids* **4**, 241 (1958).
- [47] S. Banerjee, U. Kumar, and S.-Z. Lin, Inverse faraday effect in mott insulators, *Phys. Rev. B* **105**, L180414 (2022).
- [48] T. Mizoguchi, H. Araki, and Y. Hatsugai, Higher-order topological phase in a honeycomb-lattice model with anti-kekulé distortion, *J. Phys. Soc. Jpn.* **88**, 104703 (2019).
- [49] See Supplemental Material at <http://link.aps.org/supplemental/10.1103/PhysRevB.109.104417> for the derivation of the magnon Hamiltonian, discussion on the symmetry indicator, first-order polarization by Wilson loop technique, disorder effect in the rhombus geometry, and nature of bulk and other in-gap states.
- [50] W. A. Benalcazar, T. Li, and T. L. Hughes, Quantization of fractional corner charge in  $C_n$ -symmetric higher-order topological crystalline insulators, *Phys. Rev. B* **99**, 245151 (2019).
- [51] E. Khalaf, H. C. Po, A. Vishwanath, and H. Watanabe, Symmetry indicators and anomalous surface states of topological crystalline insulators, *Phys. Rev. X* **8**, 031070 (2018).
- [52] D. Vanderbilt, *Berry Phases in Electronic Structure Theory: Electric Polarization, Orbital Magnetization and Topological Insulators* (Cambridge University Press, Cambridge, UK, 2018).
- [53] P. A. Pantaleón, R. Carrillo-Bastos, and Y. Xian, Topological magnon insulator with a kekulé bond modulation, *J. Phys.: Condens. Matter* **31**, 085802 (2019).
- [54] C. M. Purser, V. P. Bhallamudi, F. Guo, M. R. Page, Q. Guo, G. D. Fuchs, and P. C. Hammel, Spin wave detection by nitrogen-vacancy centers in diamond as a function of probe-sample separation, *Appl. Phys. Lett.* **116**, 202401 (2020).
- [55] J. Jersch, V. E. Demidov, H. Fuchs, K. Rott, P. Krzysteczko, J. Münchenberger, G. Reiss, and S. O. Demokritov, Mapping of localized spin-wave excitations by near-field brillouin light scattering, *Appl. Phys. Lett.* **97**, 152502 (2010).